

# Accretion Disc Wind Variability in the States of the Microquasar GRS 1915+105

Joseph Neilsen,<sup>1,2,3\*</sup> Andrew J. Petschek,<sup>2</sup> and Julia C. Lee<sup>2,3</sup>

<sup>1</sup>MIT Kavli Institute for Astrophysics and Space Research, Cambridge, MA 02139

<sup>2</sup>Astronomy Department, Harvard University, Cambridge, MA 02138

<sup>3</sup>Harvard-Smithsonian Centre for Astrophysics, Cambridge, MA 02138

Accepted 2011 December 5. Received 2011 November 22; in original form 2011 October 2

## ABSTRACT

Continuing our study of the role and evolution of accretion disc winds in the microquasar GRS 1915+105, we present high-resolution spectral variability analysis of the  $\beta$  and  $\gamma$  states with the *Chandra* High Energy Transmission Grating Spectrometer. By tracking changes in the absorption lines from the accretion disc wind, we find new evidence that radiation links the inner and outer accretion discs on a range of time-scales. As the central X-ray flux rises during the high-luminosity  $\gamma$  state, we observe the progressive over-ionization of the wind. In the  $\beta$  state, we argue that changes in the inner disc leading to the ejection of a transient ‘baby jet’ also quench the highly-ionized wind from the outer disc. Our analysis reveals how the state, structure, and X-ray luminosity of the inner accretion disc all conspire to drive the formation and variability of highly-ionized accretion disc winds.

**Key words:** accretion, accretion discs – stars: winds, outflows – black hole physics – instabilities – X-rays: binaries – X-rays: individual (GRS 1915+105)

## 1 INTRODUCTION

In the last two decades, *ASCA*, *Chandra*, *XMM-Newton*, and *Suzaku* have discovered a multitude of highly ionized absorbers in the X-ray spectra of black hole and neutron star X-ray binaries. In some cases, without clear evidence for blueshifts (e.g. Ebisawa 1997; Kotani et al. 1997, 2000a,b; Lee et al. 2002; Miller et al. 2004; Xiang et al. 2009), these absorbers have been attributed to hot or extended disc atmospheres. Many observations, however, provide unambiguous evidence for outflows from the accretion disc (e.g. Brandt & Schulz 2000; Schulz & Brandt 2002; Ueda et al. 2004; Miller et al. 2006a,b, 2008; Ueda, Yamaoka, & Remillard 2009; Neilsen & Lee 2009; Blum et al. 2010; Reynolds & Miller 2010; Miller et al. 2011; Neilsen, Remillard, & Lee 2011, hereafter Paper II). These results suggest that accretion disc winds may be as common as relativistic jets in accreting systems.

Of particular interest, then, is the variability of these disc winds and their role in the evolution of the accretion flow. Ionized absorbers in X-ray binaries are now known to vary on time-scales from 5 seconds (GRS 1915+105, Paper II) to 300 s (H 1743-322, Miller et al. 2006b) to ks or more (Cir X-1, Schulz & Brandt 2002; GRS 1915+105, Lee et al. 2002; Ueda et al. 2010). Furthermore, there is

mounting evidence that this variability cannot be due solely to changes in the ionizing luminosity (Lee et al. 2002; Schulz & Brandt 2002; Blum et al. 2010; Paper II), which implies that high-spectral-resolution X-ray observations of accreting X-ray binaries may be able to probe either the physical processes that link outflows to the behavior of the inner accretion flow, or inhomogeneities in the structure and density of accretion disc winds.

In a study of 10 years of *Chandra* High-Energy Transmission Grating Spectrometer (HETGS; Canizares et al. 2005) observations of GRS 1915+105, we demonstrated that the strength of absorption lines in the accretion disc wind is anticorrelated with the fractional hard X-ray flux (and the strength of the jet; Neilsen & Lee 2009, hereafter Paper I; for a preliminary discussion of the absorption lines, see Miller et al. 2008). Based on this anticorrelation and estimates of the mass loss rates in the wind and the jet, we argued that accretion disc winds may be able to suppress or quench jets by directly draining their matter supply on long time-scales. The fractional hard X-ray flux is therefore a useful indicator of both the accretion state and the physics of outflows around black holes. Yet much more can be said for GRS 1915+105, whose X-ray lightcurve exhibits at least 14 different patterns of variability (Belloni et al. 2000, hereafter B00; Klein-Wolt et al. 2002; Hannikainen et al. 2005). Many of these phenomenological patterns, which are highly structured and high-amplitude,

\* E-mail: jneilsen@space.mit.edu

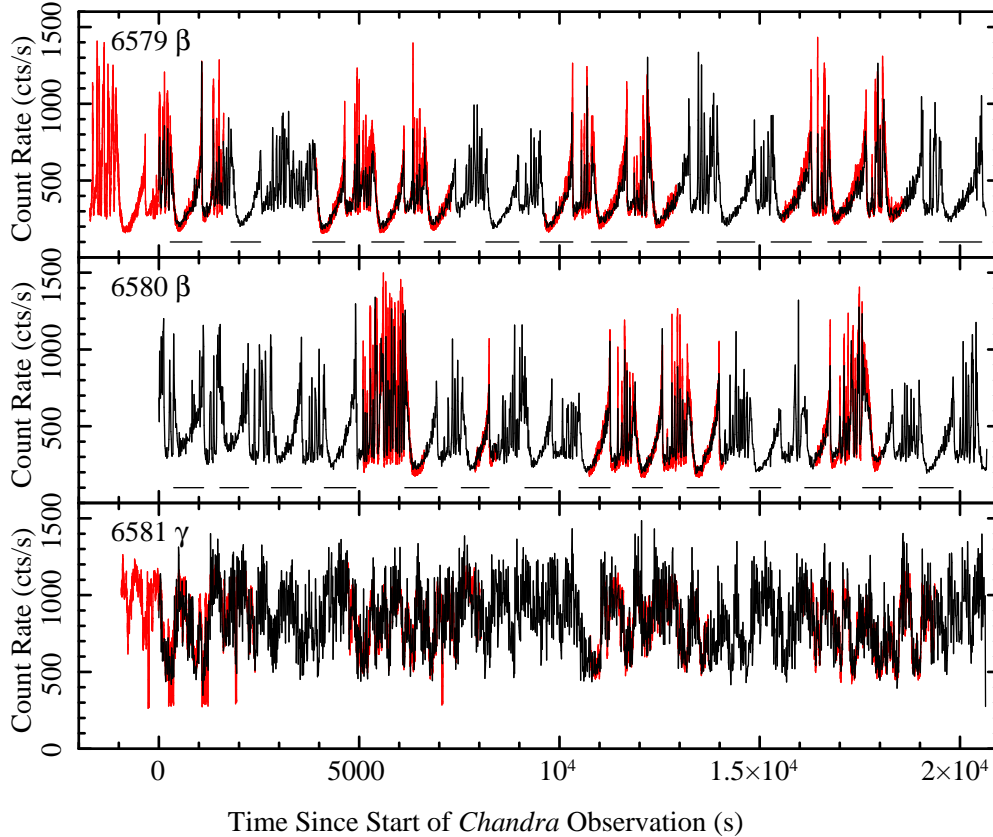


**Figure 1.** The *Chandra* (black) and *RXTE* (red) lightcurves of the  $\beta$  (top, middle) and  $\gamma$  (bottom) states. The *RXTE* lightcurves have been renormalized to match the mean *HETGS* count rate, with excellent agreement between the two missions. In the top and middle panels, we use horizontal lines to indicate the locations of the X-ray dips analysed in Section 3.1.

are interpreted as limit cycles of accretion and ejection in an unstable disc (Belloni et al. 1997; Mirabel et al. 1998; Tagger et al. 2004; Fender & Belloni 2004). In order to understand the physics linking disc winds, jets, and this fast X-ray variability, we presented the first detailed phase-resolved spectral analysis of a variability class in GRS 1915+105, using a joint *RXTE/Chandra* HETGS observation of the  $\rho$  state (Paper II). We showed for the first time that changes in the broadband X-ray spectrum produce changes in the *structure* and mass loss rate of the accretion disc wind on time-scales as short as 5 seconds. Furthermore, our analysis indicated that the wind in the  $\rho$  state may be sufficiently massive to excite long-term oscillations in the mass of the disc (Shields et al. 1986; Luketic et al. 2010). By establishing clear causal links between the X-ray oscillations and the disc wind, Paper II provides a physical mechanism that could be responsible for both the suppression of jets and (possibly) state transitions in black hole binaries.

In this paper, we continue our follow-up wind variability studies with spectral timing analysis of three additional archival *Chandra* HETGS observations of GRS 1915+105. Two of these observations (ObsIDs 6579 and 6580) fall into the  $\beta$  class, a wild  $\sim 30$ -min cycle that is associated with the production of impulsive/discrete (“baby”) radio jets (Pooley & Fender 1997; Fender et al. 1997; Mirabel et al. 1998; Eikenberry et al. 1998; Mirabel & Rodríguez 1999; Belloni et al. 2000; Klein-Wolt et al. 2002; Fender & Belloni

**Table 1.** *Chandra* HETGS observations of GRS 1915+105

Obs. ID	X-ray State	Date	Elapsed Time (ks)	$T_{\text{exp}}$ (ks)
6579	$\beta$	2005 Dec. 1	20.65	12.30
6580	$\beta$	2005 Dec. 1	21.62	12.14
6581	$\gamma$	2005 Dec. 3	20.65	9.73

2004). Each  $\beta$  cycle begins with a 10–15 minute dip in the lightcurve, which is spectrally hard and exhibits a QPO whose frequency tracks the X-ray flux (e.g. Markwardt et al. 1999; Mikles et al. 2006; Rodríguez et al. 2008b). The dip ends with a bright spike, followed by 10–15 minutes of soft, bright X-ray flares. These flares are coincident with strong optically-thin radio/infrared oscillations (baby jets), but there is an ongoing debate as to whether these discrete ejections are produced during the dip itself or at the time of the X-ray spike (Mirabel et al. 1998; Eikenberry et al. 1998; Migliari & Belloni 2003; Rothstein et al. 2005; Rodríguez et al. 2008a).

During the third observation (ObsID 6581), GRS 1915+105 exhibited irregular variability with very high X-ray flux (*RXTE* count rate  $\gtrsim 6000$  counts  $\text{s}^{-1}$  PCU $^{-1}$ ) and extremely strong red noise in the power density spectrum ( $P_\nu \sim \nu^{-2}$ ). Although we identified this as the  $\gamma$  state in Paper I and continue to refer to it thus here, this par-

ticular observation is rather unusual since it also displays significant similarities to typical  $\delta$  and  $\mu$  states. Relatively little has been said about the  $\mu$ ,  $\delta$ , and  $\gamma$  states in the literature, as none have been associated with strong radio jets (Klein-Wolt et al. 2002). However, in a study of the  $\mu$  state, Soleri, Belloni, & Casella (2008) reported the discovery of a transient low-frequency QPO, which they argue may be linked to state transitions or transient jets. This leaves open the possibility that the  $\mu/\delta/\gamma$  states exhibit physically-interesting outflow behavior, despite their weak radio flux. In this respect, these states could be similar to the  $\rho$  state, which has very low radio brightness (Klein-Wolt et al. 2002) but exhibits extreme disc wind variability and may produce short-lived jets (Paper II).

Here we address the variability of the known accretion disc wind in the *Chandra* HETGS observations of the  $\beta$  and  $\gamma$  states, whose lightcurves are shown in Figure 1. By comparing changes in the ionized absorption to changes in the X-ray flux, we show how the wind is linked to the oscillations in the inner disc. The paper is organized as follows: in Section 2 we describe our observations and data reduction. In Section 3 we perform spectral analysis of the wind in the  $\beta$  state with the *Chandra* HETGS and *RXTE* PCA; in 4 we use the HETGS to study the wind in the  $\gamma$  state. We discuss the implications of our results in Section 5.

## 2 OBSERVATIONS AND DATA REDUCTION

GRS 1915+105 was observed with the *Chandra* HETGS on 2005 December 1 (01:45:09 UT and 18:41:30 UT) and Dec 3 (16:26:06 UT) for 20.65 ks, 21.62 ks, and 20.65 ks, respectively. The data were taken in Continuous Clocking Mode, which has a time resolution of 2.85 ms, in order to mitigate photon pileup. However, due to the high X-ray flux the observations suffered from severe telemetry saturation, so that the good exposure times for these observations were only 12.30 ks, 12.14 ks, and 9.73 ks (details in Table 1).

We reduce and barycentre-correct the *Chandra* data using standard tools from the CIAO analysis suite, version 4.3. We use the order-sorting routine to remove the ACIS S4 readout streak, since the *dstreak* tool can introduce spectral artefacts for bright continuum sources like GRS 1915+105. After reprocessing and filtering, we extract High-Energy Grating (HEG) spectra and create grating responses. For the  $\gamma$  observation (ObsID 6581), we find that the detected position of the 0<sup>th</sup>-order image results in an offset of  $-44$  eV between the HEG  $-1$  and HEG  $+1$  orders (measured from the centroid of the Fe XXVI line at  $\sim 7$  keV). Shifting the position of the 0<sup>th</sup>-order image to the nominal source position results in an offset of  $36$  eV, so we take the average of the detected position and the nominal position as the true location of the 0<sup>th</sup>-order image on the CCD. The resulting position error from this average is less than  $0.1$  pix, so the associated uncertainties in the wavelength calibration are smaller than our uncertainty in the line centroids. We also extract 10-second lightcurves with *dmextract*.

Due to incomplete calibration of Charge-Transfer Inefficiency (CTI) in CC mode, there is some wavelength-dependent disagreement in the continuum flux between spectral orders of the HEG (and the MEG, which we do not consider here because of its lower spectral resolution). For this reason, it is not currently possible to fit a physical continuum model to the HETGS data. Instead, we fit the individ-

ual spectra with polynomials to model the local continuum and use Gaussians for line features found in the combined residuals.

During the *Chandra* observations, *RXTE* made pointed observations of GRS 1915+105, lasting 23.1 ks, 13.7 ks, and 21.7 ks (elapsed), with exposure times of 13.2 ks, 7.2 ks, and 13.6 ks, respectively. We select all available data subject to the following constraints: (1) the Earth-limb elevation angle is above  $3^\circ$ ; (2) the spacecraft is outside the South Atlantic Anomaly; (3) the offset angle from GRS 1915+105 is less than  $0.02^\circ$ . In this paper, we analyse the data from the Proportional Counter Array (PCA), which covers the 2–60 keV band, in order to verify and supplement the variability detected by *Chandra*. For timing analysis, we make use of the data from the binned mode B\_8ms\_16A\_0.35\_H4P, which covers the 2.0–14.8 keV band at 7.8 ms time resolution, and the event mode E\_16us\_16B\_36\_1s, which covers the 14.8–60 keV band at  $15.3 \mu\text{s}$  time resolution. We extract and combine 1-second background subtracted lightcurves from each of these modes. For comparison to the *Chandra* data, we barycentre the *RXTE* lightcurves. For spectral analysis, we extract Standard-2 129-channel spectra from relevant time intervals (see Section 3 and Figure 1). We restrict our analysis to the 3–45 keV top layer spectrum of PCU-2, which is best calibrated. We assume 0.6% systematic errors. Although these states exhibit some strong variability on time-scales shorter than the 16-second bins of the Standard-2 data, our goal is to use the spectra to understand the ionization of the wind, not to characterize physical variability in the accretion disc and corona.

## 3 THE $\beta$ STATE

In this section, we explore the variability and dynamical evolution of the accretion disc wind in the  $\beta$  state. Here, links between the extreme X-ray variability and the disc wind are particularly interesting given the association of the  $\beta$  state with transient jets and disc-jet interactions. Previously, we analysed the average spectrum of these two (ObsIDs 6579 and 6580; Table 1) joint RXTE/*Chandra* observations of GRS 1915+105 in the  $\beta$  state (Paper I). We found the average RXTE continuum during each of these observations to be relatively soft, with  $\sim 79\%$  of the 3–18 keV X-ray luminosity emitted below 8.6 keV ( $L_X \sim 6 \times 10^{38}$  ergs s<sup>-1</sup>). In both time-averaged high-resolution X-ray spectra from the HETGS, we detected an FeXXVI Ly $\alpha$  absorption line from the accretion disc wind. This feature had equivalent widths of  $W_0 = 13.3^{+3.0}_{-2.9}$  eV and  $19.3^{+3.2}_{-3.5}$  eV in observations 6579 and 6580, respectively; the corresponding blueshifts were  $910^{+430}_{-390}$  km s<sup>-1</sup> and  $1100^{+300}_{-360}$  km s<sup>-1</sup>. In what follows, we use the known properties of the  $\beta$  state to extract high-resolution X-ray spectra corresponding to physically-interesting intervals of this unusual oscillation. We compensate for severe telemetry saturation (leading to reduced counts, Section 2; Table 1) by fitting both observations 6579 and 6580 jointly. All spectral fitting is done from 5–8 keV in ISIS (Houck & Denicola 2000; Houck 2002). We assume a distance and inclination of  $D = 11.2$  kpc and  $i = 66^\circ$  (Fender et al. 1999); we fix  $N_H = 5 \times 10^{22}$  cm<sup>-2</sup> (Lee et al. 2002 and references therein).

In general, choosing time intervals for spectral timing analysis is difficult, but the  $\beta$  lightcurve is easily divided into two sections with different physical properties: (1) the

**Table 2.** X-ray absorption lines in GRS 1915+105

State	Interval	$F_{5-8}$	Line	$E_0$ (keV)	$E_{\text{obs}}$ (keV)	$\Delta v_{\text{shift}}$ (km s <sup>-1</sup> )	$\sigma_v$ (km s <sup>-1</sup> )	Flux	$W_0$ (eV)
$\beta$	Dip	$6.0 \pm 0.5$	Fe XXVI	6.961	$6.993^{+0.009}_{-0.012}$	$-1340^{+520}_{-400}$	$< 1310$	$1.9^{+0.7}_{-0.6}$	$11.3^{+4.1}_{-3.8}$
			Fe XXV	6.700	$6.730^a$	$-1340^a$	= Fe XXVI	$< 0.8$	$< 4.8$
	Flare	$7.6 \pm 0.4$	Fe XXVI	6.961	$6.982^{+0.006}_{-0.005}$	$-900^{+230}_{-240}$	$660^{+230}_{-240}$	$5.4 \pm 0.8$	$26.0^{+3.8}_{-3.9}$
			Fe XXV	6.700	$6.718^{+0.010}_{-0.008}$	$-780^{+360}_{-450}$	= Fe XXVI	$2.7 \pm 0.7$	$11.4^{+2.8}_{-3.0}$
	$\beta_1$	$4.6 \pm 0.4$	Fe XXVI	6.961	$6.986^{+0.009}_{-0.010}$	$-1060^{+420}_{-390}$	$1140^{+360}_{-300}$	$5.2 \pm 0.1$	$42.2^{+8.1}_{-8.1}$
			Fe XXV	6.700	$6.71 \pm 0.01$	$-560^{+470}_{-590}$	= Fe XXVI	$3.5^{+0.9}_{-1.0}$	$24.6^{+6.6}_{-6.9}$
	$\beta_2$	$6.1 \pm 0.5$	Fe XXVI	6.961	$6.984^{+0.012}_{-0.007}$	$-950^{+310}_{-520}$	$< 790$	$3.8 \pm 0.1$	$22.9^{+5.9}_{-6.2}$
			Fe XXV	6.700	$6.718^{+0.013}_{-0.009}$	$-800^{+390}_{-560}$	= Fe XXVI	$2.1 \pm 0.9$	$11.3^{+4.8}_{-4.8}$
	$\beta_3$	$13.9 \pm 0.3$	Fe XXVI	6.961	$6.980^{+0.008}_{-0.005}$	$-780^{+220}_{-360}$	$< 910$	$8.6^{+1.9}_{-2.0}$	$22.3^{+4.9}_{-5.1}$
			Fe XXV	6.700	$6.718^a$	$-780^a$	= Fe XXVI	$3.2^{+1.7}_{-1.8}$	$7.5^{+3.9}_{-4.1}$
	$\gamma_1$	$18.8 \pm 1.5$	Fe XXVI	6.961	$6.985 \pm 0.008$	$-1020^{+320}_{-330}$	$700^{+410}_{-430}$	$11.6 \pm 2.8$	$21.3 \pm 5.1$
			Fe XXV	6.700	$6.723^a$	= Fe XXVI	= Fe XXVI	$3.5^{+2.2}_{-2.3}$	$5.9^{+3.7}_{-3.9}$
$\gamma$	$\gamma_2$	$22.5 \pm 2.0$	Fe XXVI	6.961	$6.983^{+0.009}_{-0.008}$	$-920^{+350}_{-390}$	$980^{+540}_{-410}$	$14.1^{+3.4}_{-3.0}$	$21.4^{+5.2}_{-4.6}$
			Fe XXV	6.700	$6.721^a$	= Fe XXVI	= Fe XXVI	$< 5.7$	$< 7.9$
	$\gamma_3$	$24.8 \pm 2.2$	Fe XXVI	6.961	$6.990 \pm 0.007$	$-1240 \pm 300$	$1000^{+420}_{-350}$	$19.0^{+3.7}_{-3.4}$	$26.4^{+5.1}_{-4.8}$
			Fe XXV	6.700	$6.728^a$	= Fe XXVI	= Fe XXVI	$< 4.5$	$< 5.7$
	$\gamma_4$	$26.4 \pm 2.3$	Fe XXVI	6.961	$6.998 \pm 0.007$	$-1550^{+300}_{-280}$	$790^{+490}_{-680}$	$17.6^{+3.9}_{-3.7}$	$23.1^{+5.1}_{-4.8}$
			Fe XXV	6.700	$6.735^a$	= Fe XXVI	= Fe XXVI	$< 6.6$	$< 7.6$
	$\gamma_5$	$28.3 \pm 2.2$	Fe XXVI	6.961	$6.996^{+0.008}_{-0.010}$	$-1490^{+440}_{-340}$	$< 1330$	$12.9^{+2.8}_{-3.2}$	$16.0^{+3.5}_{-4.0}$
			Fe XXV	6.700	$6.734^a$	= Fe XXVI	= Fe XXVI	$< 6.5$	$< 7.4$

Errors quoted are 90% confidence ranges for a single parameter unless otherwise stated. State: X-ray variability type in the classification of B00. Interval: line parameters are reported for different flux levels and time intervals (see text for more details).  $F_{5-8}$ : 5–8 keV (absorbed) continuum flux in units of  $10^{-9}$  photons s<sup>-1</sup> cm<sup>-2</sup>, with errors given by the standard deviation between the HEG  $\pm 1$  orders;  $E_0$ : rest energy;  $E_{\text{obs}}$ : measured energy;  $\Delta v_{\text{shift}}$ : measured Doppler velocity;  $\sigma_v$ : line width; Flux: measured absorbed line flux in units of  $10^{-3}$  photons s<sup>-1</sup> cm<sup>-2</sup>;  $W_0$ : line equivalent width.

<sup>a</sup> Since the Fe XXV line is not very significant during this interval, we tie its velocity to that of Fe XXVI.

long, hard, discrete jet-producing dip and (2) the subsequent period of bright flaring. Examination of the  $\beta$ -state X-ray lightcurves in the literature and in our data indicates that the hard dip is bracketed on the left by the last bright flare of the preceding flaring interval, and on the right by peak or falling edge of the X-ray spike. Using the *Chandra* lightcurve and the PCA lightcurve where available, we hand-select the dip and flare intervals accordingly. The resulting GTIs are shown underneath the X-ray lightcurves in the top and middle panels of Figure 1.

### 3.1 *Chandra* HETGS

Applying these GTIs to the *Chandra* observations, we extract high-resolution spectra corresponding to the dip and flaring intervals. We show the resulting spectra in Figure 2. As discussed in Section 2, we model the *Chandra* X-ray continuum with polynomials to account for calibration uncertainties. This technique effectively isolates narrow absorption lines by characterizing the local continuum. We use Gaussian lines to measure the properties of the ionized iron absorption lines during each time interval; our results are shown in Table 2.

Both Figure 2 and Table 2 reveal clear differences between the accretion disc wind during the flare and dip inter-

vals. From Figure 2, it can be seen that during the flares (top panel), we detect strong absorption lines from both Fe XXVI (Ly $\alpha$ : 1s – 2p, 6.96 keV) and Fe XXV (He $\alpha$ : 1s<sup>2</sup> – 1s2p, 6.7 keV). The significance of the Fe XXV and Fe XXVI lines ( $\sim 6\sigma$  and  $\sim 11\sigma$ ) indicates a relatively strong, highly-ionized outflow. During the dip (middle panel), Fe XXVI is much weaker and Fe XXV is not significant at all, although it can be seen as a faint blip in the residuals (bottom panel). Although the 5–8 keV continuum flux decreases (Table 2) from the flares to the dip, the bolometric luminosity remains roughly constant (Section 3.2).

Interestingly, Table 2 shows that aside from the reduction in line flux, there are few if any quantitative differences between the iron absorbers during these two parts of the  $\beta$  cycle. During the flares, the wind is blueshifted by  $900^{+240}_{-230}$  km s<sup>-1</sup> and has a line-of-sight velocity dispersion of  $\sigma_v = 660^{+230}_{-240}$  km s<sup>-1</sup>. In the spectrally-hard dip, the blueshift is  $1340^{+400}_{-520}$  km s<sup>-1</sup> and the lines are unresolved, but we constrain the velocity dispersion to be  $< 1310$  km s<sup>-1</sup>. These results are consistent with the long-term behavior of the wind that we reported in Paper I. Perhaps the most surprising result, however, is that despite the low significance of Fe XXV in the dip, the dip and flare spectra are statistically consistent with a constant Fe XXV/Fe XXVI ra-

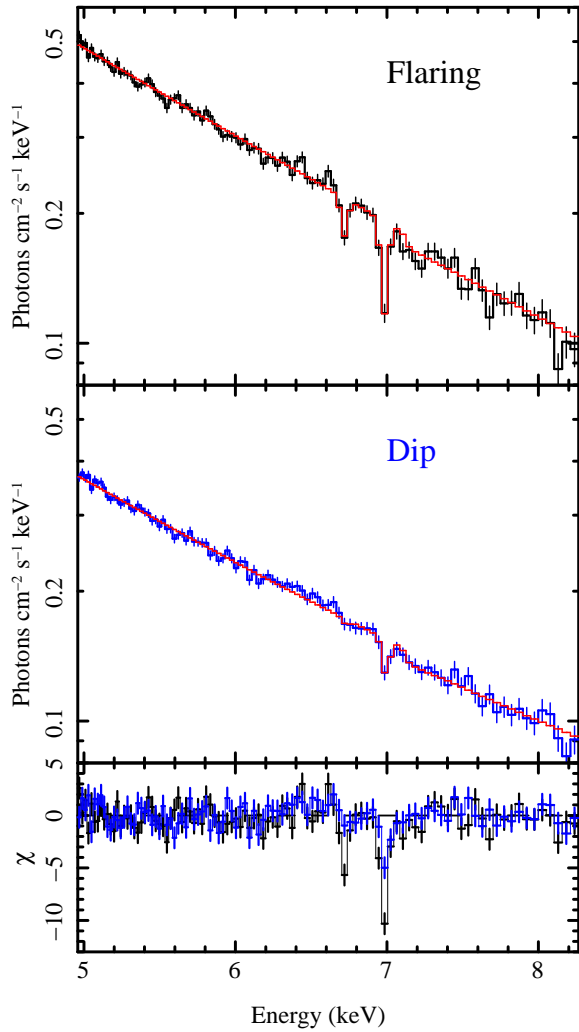


**Figure 2.** The *Chandra* HETGS spectra and residuals for the flaring (top panel) and dip (middle panel) intervals of the  $\beta$  state of GRS 1915+105. We detect strong absorption lines from Fe XXVI during both time periods, and Fe XXV during the X-ray flaring. These spectra include portions of observations 6579 and 6580, coadded to improve our sensitivity. The residuals are calculated with the line normalizations set to zero.

tio. This suggests that the ionization state of the plasma in the wind might not vary from the dip to the flares, despite known changes in the hardness of the X-ray spectrum (Section 3.2).

We can substantiate this claim using a simple multiplicative Gaussian model based on chapter 9 of Draine (2011) that replaces the line flux parameter with the ion column density. First, we fit both phases of the cycle separately, allowing the Fe XXVI/Fe XXV ratio to vary between the dip and the flares. Then we fit them together, requiring both intervals to have the same Fe XXVI/Fe XXV ratio and line width. With the line ratios free, we achieve  $\chi^2/\nu = 884.0/791 = 1.12$ ; with the line ratios and widths tied together, we obtain the same reduced  $\chi^2 = 885.8/793 = 1.12$ . In other words, there is no evidence (at the level of our line detections) that the ionization state of the wind changes between the dip and the flare.

Using the results from our “tied” model, we find that the average Fe XXVI/Fe XXV ratio is  $r = 0.17^{+0.06}_{-0.05}$ ; the

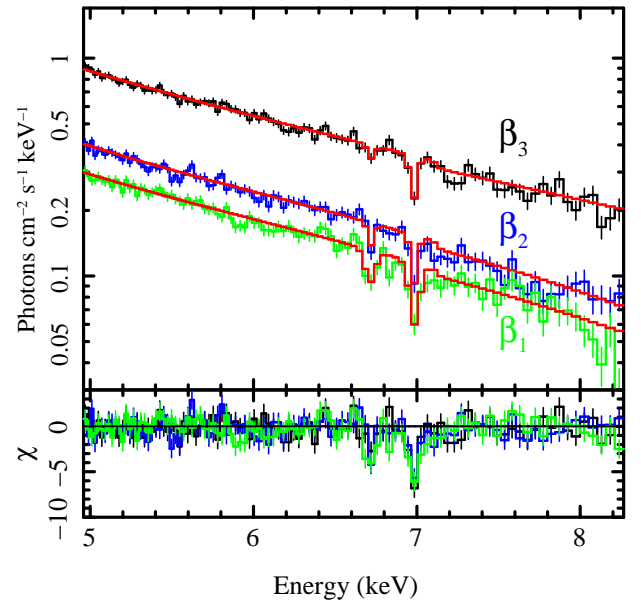


**Figure 3.** *Chandra* HETGS flux-resolved spectra and residuals for the flaring interval of the  $\beta$  state. As discussed in the text, the weakening of the Fe XXV line can be taken as an indication that the ionization of the wind may increase slightly with the continuum flux during the flares.

Fe XXVI column density is  $N_{\text{Fe } 26} = 2.6^{+0.9}_{-0.8} \times 10^{17} \text{ cm}^{-2}$  during the dip and  $N_{\text{Fe } 26} = 8.0^{+1.6}_{-1.3} \times 10^{17} \text{ cm}^{-2}$  during the flares. To convert from the ion column density to equivalent hydrogen columns, we assume elemental abundances from Wilms, Allen, & McCray (2000). Assuming only the ionic abundances of Fe XXV and Fe XXVI are non-zero, then these results imply an equivalent hydrogen column density in the wind of  $N_{\text{H}} = 1.0 \pm 0.3 \times 10^{22} \text{ cm}^{-2}$  during the dip and  $N_{\text{H}} = 3.0^{+0.6}_{-0.5} \times 10^{22} \text{ cm}^{-2}$  during the flares. We obtained similar results with photoionization models of the disc wind in the  $\rho$  state (Paper II), so we believe our simple measure of  $N_{\text{H}}$  here is plausible. We conclude that the column density of the wind decreases significantly from the flares to the dip, while its bulk dynamical and ionization properties remain constant.

We can also ask whether or not the absorption lines vary within the flaring phase (our S/N is too low to perform a similar analysis of line variability in the dip). Using the *Chandra* lightcurve, we create new GTI files to divide the flare phase into three flux bands with roughly equal exposure times. The resulting spectra (see Figure 3) reveal significant differences in the wind between the lowest flux levels and the highest flux levels. Visible differences include apparent decreases in the equivalent widths and line widths, and a decrease in the strength of the Fe XXV line relative to Fe XXVI with increasing continuum flux. There is no evidence for variations in the velocity of the wind, but the changes in the line width and the Fe XXV/Fe XXVI ratio are marginally significant at 90% confidence (Table 2). Thus it appears that the ionization state or density of the wind may be somewhat sensitive to the luminosity on short time-scales.

### 3.2 RXTE PCA

With sensitive coverage out to 45 keV, *RXTE* PCA spectra can also provide valuable insight into variable ionization processes, so we extract PCA spectra for the dip and flaring phases with the same GTIs used for the HETGS (see

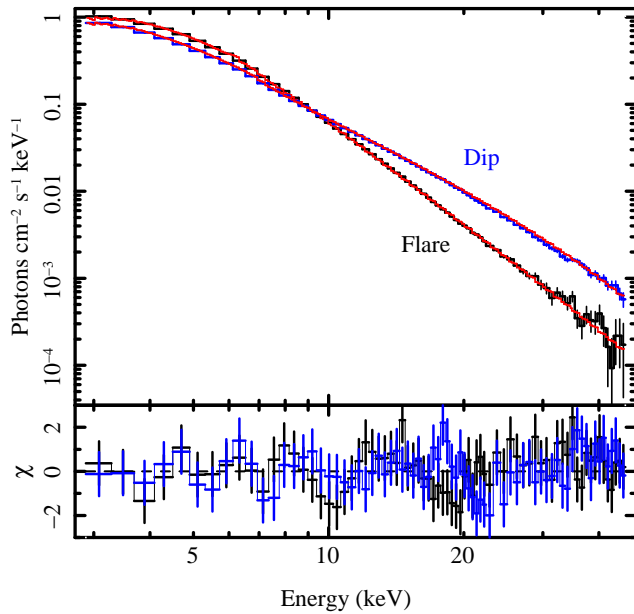


**Figure 4.** *RXTE* PCA spectra of the  $\beta$ -state dip and flare, for comparison to Figure 2. The dip spectrum is notably harder than the spectrum of the flaring phase, but the 1 eV – 1 MeV luminosities are comparable at  $10^{39}$  ergs s $^{-1}$ . This suggests that the changes in the X-ray absorber may require variations in the density or geometry of the wind (see Section 5.1).

Figure 1). Our purpose here is not to explore the variability of the accretion disc and corona, which has been done for the  $\beta$  state (e.g. Migliari & Belloni 2003; Rothstein et al. 2005), but to capture the average shape of the ionizing spectrum. With typical wind densities around  $10^{12}$  cm $^{-3}$  (Lee et al. 2002; Ueda et al. 2009; Neilsen et al. 2011), the recombination time-scale is of the order of a few tenths of ms (Kallman et al. 2009). Thus our treatment of the average spectrum is justified because the wind can effectively respond instantly to changes in the ionizing spectrum.

We find that the average dip spectrum can be reproduced with a model consisting of cold absorption (**tbabs**; Wilms et al. 2000), a disc component (**ezdiskbb**; Zimmerman et al. 2005), a Comptonized component (**nthcomp**; Zdziarski, Johnson, & Magdziarz 1996; Życki, Done, & Smith 1999), and an emission line in the 5–7 keV range (**egauss**). The disc is cool ( $\sim 0.75$  keV) with a normalization ( $\sim 800$ ) that implies an inner radius around 120 km. The photon index is  $\Gamma \sim 2.5$ , and the electron temperature is  $\sim 12$  keV; we tie the seed photon temperature to the disc temperature. During the flaring interval, we replace **nthcomp** with a high-energy cutoff (**highcut**) and **simpl**, a convolution model that takes a seed spectrum and scatters a fraction of the photons into a power law (Steiner et al. 2009). Our fits to the average flare spectrum imply a slightly hotter, smaller disc ( $T \sim 1.1$  keV,  $R \sim 100$  km), a steeper power law ( $\Gamma \sim 3.8$ ) comprising  $\sim 60\%$  of the photon flux, and an  $e$ -folding energy  $> 75$  keV (we set the cutoff energy to zero). The fit parameters themselves must be interpreted cautiously given the strong variability in the flare and dip, but our models provide a good description of the spectra ( $\chi^2/\nu = 222.9/264$ ; see Figure 4).

Again, our primary interest is in the influence of the broadband continuum on the ionization of the wind, particularly the strength of the Fe XXV absorption line. To that

end, we integrate our models over the Fe XXV photoionization cross-section (Verner et al. 1996) to determine the expected ionizing flux. In the flares, we find  $\sim 1.3 \times 10^{-3}$  ionizing photons s $^{-1}$  cm $^{-2}$ ; during the dip, we find  $\sim 20\%$  more ionizing photons ( $\sim 1.5 \times 10^{-3}$  photons s $^{-1}$  cm $^{-2}$ ). Both spectra have 0.001–1000 keV luminosities near  $10^{39}$  ergs s $^{-1}$ . Since the luminosity and ionizing flux changes are modest, it is conceivable that the ionization state of the wind remains constant between the dip and the flares. However, the impact of the ionizing flux on the lines also depends on the changing density and geometry of the wind, as well as its characteristic distance from the continuum source (see Paper II and references therein). We explore these factors in more detail in Section 5.1.

#### 4 THE $\gamma$ STATE

In this section, we turn our attention to the variability of the accretion disc wind in the  $\gamma$  state (ObsID 6581; Table 1). In Paper I, we reported the average *RXTE* continuum to be very soft, with  $\sim 82\%$  of the 3–18 keV X-ray luminosity emitted below 8.6 keV ( $L_X \sim 13 \times 10^{38}$  ergs s $^{-1}$ ). In the time-averaged *Chandra* HETGS spectrum, we detected an Fe XXVI absorption line with an equivalent width of  $-21.9^{+2.2}_{-2.7}$  eV and a blueshift of  $1000^{+220}_{-240}$  km s $^{-1}$ .

Although no significant jet activity has been reported in the  $\gamma$ ,  $\delta$ , or  $\mu$  states (Klein-Wolt et al. 2002), the strong red-noise variability (bottom panel of Figure 1) may still provide clues about the links between radiation and outflows in accreting X-ray binaries. In what follows, we discuss the variability of the wind in this state, which is largely unexplored.

The erratic variability here poses some difficulties for grating studies, since phase-folding (e.g. Neilsen et al. 2011) and filtering on hardness-hardness-intensity diagrams (Soleri et al. 2008) are not possible. These difficulties are compounded by the telemetry saturation discussed in Section 2. The simplest approach, dividing the observation into several time intervals, reveals no statistically-significant variability in the wind, so we opt to extract flux-resolved spectra based on the count rate in the *Chandra* lightcurve. Because the exposure time and S/N are already relatively small, we use a sliding box (e.g. Schulz & Brandt 2002; Neilsen et al. 2011) to create five spectra, each covering roughly one-third of the count rate distribution (with overlap). While this method alleviates the difficulty in selecting physically-motivated GTIs, it does create some overlap between consecutive spectra. We only use statistically-independent spectra for our variability calculations.

We show the three statistically-independent spectra ( $\gamma_1$ ,  $\gamma_3$ , and  $\gamma_5$ ) in Figure 5; all three spectra contain a strong Fe XXVI line with a blueshift of 1000 – 1500 km s $^{-1}$ . In contrast to the  $\beta$ -state spectra, here there is little evidence for absorption by Fe XXV (we ignore the weak features near 6.6–6.7 keV in  $\gamma_3$  and  $\gamma_5$  because they do not show up in both of the HEG  $\pm 1$  orders). The absence of Fe XXV is plausible from an ionization perspective, given the high continuum flux in the  $\gamma$  state. Our multiplicative Gaussian model (Section 3.1) indicates that  $N_{\text{Fe } 26} \sim 6 \times 10^{17}$  cm $^{-2}$ . If all the iron is locked up in Fe XXVI (again, plausible because we do not observe any other lines), this value of  $N_{\text{Fe } 26}$  implies an equivalent hydrogen column density of  $N_H \sim 2 \times 10^{22}$  cm $^{-2}$ . However, this hydrogen column should be regarded



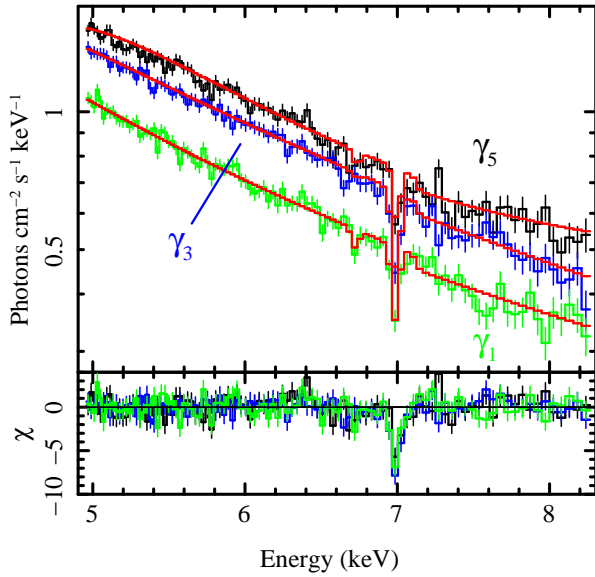


**Figure 5.** The *Chandra* HETGS flux-resolved spectra and residuals for three distinct intervals in the  $\gamma$  state. The continuum level changes, but the lines are very similar during these intervals. However, the complicated relationship between the absorbed line flux and the continuum (Section 4) indicates that photoionization effects are still important at these high luminosities.

as a lower limit, since there could be a significant population of fully-ionized iron (which would increase the total iron column density *without* affecting the lines).

As for the variability of the wind in the  $\gamma$  state, it is clear from Figure 5 that the continuum flux is variable, but the lines themselves are difficult to distinguish because they have similar significance, absorbed fluxes, and blueshifts. From Table 2, however, the Fe XXVI line flux is highest at intermediate luminosities, and the equivalent width drops at the highest luminosities. We rule out a constant line flux at the  $\sim 97\%$  confidence level. The variation of the equivalent width between all three spectra is not particularly significant, but the decrease in  $W_0$  in  $\gamma_5$  relative to  $\gamma_1$  and  $\gamma_3$  has a formal significance of  $\sim 97\%$ . In general, the lines do not appear to track the continuum flux directly, and so may be subject to other influences (Section 5).

## 5 DISCUSSION

In GRS 1915+105, the accretion disc wind is now known to vary on time-scales ranging from a few seconds to (nearly) decades. This variability appears particularly in the column density and ionization state of the wind, but is also evident in the gas density, velocity, and velocity dispersion. In the rest of this section, we discuss the implications of our results for the complex relationship between the properties of the wind and the luminosity of the central X-ray source, which is responsible not only for driving the wind, but also for ionizing it (e.g. Begelman et al. 1983; Proga & Kallman 2002; Neilsen et al. 2011).

### 5.1 The $\beta$ state: dip vs. flare

First we consider the dip and flare intervals of the  $\beta$  state described in Section 3.1. To recap briefly, we find that when moving from the flaring phase into the hard X-ray dip, the column density of the wind decreases significantly ( $\sim 3\times$ ),

while its velocity and velocity dispersion remain constant. Furthermore, the ionization state of the absorber does not appear to change despite changes in the shape of the ionizing spectrum. We argued in Section 3.2 that changes in the density or geometry of the wind might therefore be important in determining the properties of the absorber.

For a toy model of this variability, suppose that the wind is launched from the disc as a sphere expanding with constant velocity  $v$ , and suppose further that the wind is launched solely during the bright, soft, X-ray flares. In other words, no wind is driven off the disc during the hard X-ray dip. For simplicity, we assume the wind is spherical, but as long as its solid angle is roughly constant this toy model will still apply. By the end of the flaring phase of the  $\beta$  cycle, which we define as  $T = 0$ , this sphere has a characteristic radius  $R_0$  that is comparable to the typical launch radius of the wind (see the top panel of Figure 6). During the course of a flaring interval, the accretion disc launches  $N$  particles into the wind, so that the expected column density is

$$N_{H0} = \frac{N}{4\pi R_0^2}. \quad (1)$$

During the dip, an average time  $\Delta T$  later, when the characteristic radius of the wind is

$$R_1 = R_0 + v\Delta T, \quad (2)$$

the expected column density is

$$N_{H1} = \frac{N}{4\pi R_1^2} \quad (3)$$

$$= \frac{N}{4\pi (R_0 + v\Delta T)^2}. \quad (4)$$

Given the ratio of column densities in and out of the hard X-ray dip, as well as the wind speed and  $\Delta T$ , we can solve for the wind launch radius  $R_0$ :

$$R_0 = \frac{v\Delta T}{\Phi - 1}, \quad (5)$$

where  $\Phi = \sqrt{N_{H0}/N_{H1}}$ . Using the values reported in Section 3.1, Table 2, and an average mid-flare to mid-dip  $\Delta T = 626$  s, we calculate  $R_0 = (8 \pm 3) \times 10^{10}$  cm. The error comes from propagating  $1\sigma$  uncertainties for each of the measured quantities through Equation (5). The implied gas density in the wind is  $n_e = (1.4 \pm 0.5) \times 10^{12}$  cm $^{-3}$ , and the expected ionization parameter is around  $10^{5.2}$  ergs cm s $^{-1}$ . This is rather high for the observed lines, but could be reduced if the wind is clumpy or accelerates in the dip, as hinted at in Table 2. The average mass loss rate in the typical  $\sim 800$  s flare phase is  $\dot{M}_{\text{wind}} = (7 \pm 5) \times 10^{18}$  g s $^{-1}$ ; the instantaneous mass loss rate from the disc could be significantly higher if the wind is only launched during a fraction of the flare phase, or if the ionic abundance of completely-ionized iron is not negligible during the dip.

Of course, the fact that this toy model returns sensible results does not imply or require that it is correct. We could alternately suppose, for example, that the wind is produced at a constant rate throughout the cycle. In this case, we can replace  $\Phi$  in equation 5 with  $\chi = \Phi * \sqrt{1 + \Delta T_{\text{dip}}/\Delta T_{\text{flare}}}$ . Here the  $\Delta T$ s represent the duration of the dip and flare intervals. For our data,  $\Phi \sim 1.7$  and  $\chi \sim 2.6$ , so this modification to our model reduces  $R_0$  by a factor of  $\sim 2$ . The density  $n_e$  increases by a similar factor, but because the ionization parameter  $\xi$  scales with  $R^{-2}$ , the modified model

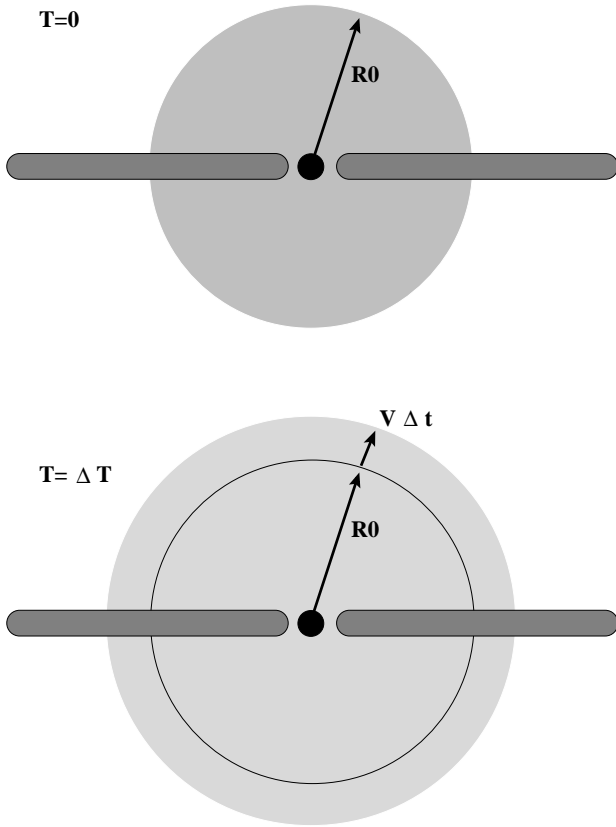


**Figure 6.** Toy model for the evolution of the column density in the  $\beta$  state of GRS 1915+105. (TOP): the flaring interval, where the (spherical) wind has characteristic radius  $R_0$  and a high column density (indicated by dark shading). (BOTTOM): during the dip, a time  $\Delta T$  later, the wind has expanded and its column density has decreased accordingly (lighter shading). In Section 5.1, we use this model and our measurements of the column density to estimate  $R_0 \approx 8 \times 10^{10}$  cm.

implies even more ionization than our original model (where the wind shuts off in the dip). Overall, both are reasonable, but the excess ionization in the modified (constant wind) model is potentially problematic. Again, the ionization parameter could be reduced if the wind is clumpy, but the modified model requires an even clumpier wind than our original model, since the ionization parameters are  $\xi_{\text{modified}} \approx 2\xi_{\text{original}}$ . Furthermore, we know from previous work that hard X-ray spectra (similar to that observed in the dip) tend to indicate activity in jets rather than disc winds (e.g. Klein-Wolt et al. 2002; Fender, Belloni, & Gallo 2004; Neilsen & Lee 2009 and references therein). This would lead us to the prediction that the hard dip would be more likely to produce a jet than a wind. For these reasons, we suggest that our original model for the wind variability in the  $\beta$  state is preferable, and that the wind actually does turn off during the dip.

As in our previous work on the persistent properties of the wind on long time-scales and its variability on short time-scales (Neilsen & Lee 2009; Neilsen et al. 2011; see also Luketic et al. 2010), our results are consistent with a wind driven primarily via a combination of Compton heating of the outer accretion disc and radiation pressure on free electrons. Furthermore, our results hint at a unifying process

driving the wind. In the heartbeat ( $\rho$ ) state, which consists of bright X-ray pulses every  $\sim 50$  seconds, we found that each X-ray pulse heats up a large region of the disc and drives new gas into the line of sight (Neilsen et al. 2011). Since the flares in the  $\beta$  state are similar to the pulses in the heartbeat state (as will be demonstrated definitively in our forthcoming analysis of a new *Chandra*, *RXTE*, *EVLA* and *Gemini* campaign; Neilsen et al. 2012, in preparation), the mechanisms producing the winds are likely similar as well.

Yet the wind in the  $\beta$  state also exhibits a critical difference from the wind in the heartbeat state, for our toy model of the  $\beta$  state suggests that the wind actually shuts off during the hard X-ray dip. We find no evidence in the line ratios for over-ionization of the absorber during the dip, and the ionizing flux is comparable during both phases of the cycle. It seems improbable that such modest changes in the ionizing and bolometric luminosities could lead to enough over-ionization to reduce the apparent wind column density so significantly. Thus we conclude that there is a long interval where *no wind is launched from the disc*, a fact that is rather counterintuitive because the wind absorption lines never fade completely. But during the dip, we actually detect the remnant of the wind launched by prior flares (in the form of significantly weaker absorption lines).

This result poses an intriguing puzzle: why doesn't the disc produce any wind during the X-ray dip? Our data do not provide any clear answers to this question, but the dip and the flares have similar average X-ray luminosities, so it seems improbable that the wind is quenched solely due to changes in the heating or energetics of the outer disc.

One possibility is that the highly-ionized wind in GRS 1915+105 is primarily produced by short but intense pulses of radiation, as observed in the heartbeat and  $\beta$  states. If this impulsive driving process launches partially- or temporarily-ballistic parcels of gas into the line of sight, it might explain how the Fe XXVI/Fe XXV ratio can remain roughly constant over a large range in luminosity (see Kallman & Bautista 2001): ionization would only become important as the wind rises well above the disc. Along this line of reasoning, it is interesting that Miller et al. (2006b) detected a wind with very similar ionization properties in H1743-322 while the source was undergoing moderate  $\sim 300$  s oscillations. Still, a general link between wind formation, ionization, and X-ray variability leaves much to be explained. For example, if variability is important, why are these winds rarely observed during X-ray hard states, where the rms X-ray variability is high? What determines whether the wind is highly ionized, as in H1743-322 and the  $\beta$ ,  $\gamma$ , and  $\rho$  states of GRS 1915+105, or cooler with many lines, as in GX 13+1 (Ueda et al. 2004), GRO J1655-40 (Miller et al. 2006a), and the  $\phi$  state of GRS 1915+105 (Ueda et al. 2009)?

With these questions unanswered, a simpler explanation for the absence of a wind is that the outer accretion disc is shadowed during the hard X-ray dip and does not receive the full irradiating force of the X-ray luminosity. This could be possible if, for example, the inner disc is puffed up during the dip, so that low inclinations are shielded from the X-ray emission (see also Ponti et al. 2011). In this explanation we find an exciting link to the formation of jets, since it is believed that steady jets may require geometrically-thick discs (e.g. Meier 2001). To be clear, the  $\beta$  state produces discrete synchrotron blobs (baby jets; Fender et al. 1997;



Pooley & Fender 1997; Mirabel et al. 1998), not the compact, flat-spectrum jets for which the thick disk theory was developed. However, a thick disk may also be required to produce other kinds of jets, like those observed after the hard dip in the  $\beta$  state. Whether the baby jet is launched continuously during the hard dip (e.g. Klein-Wolt et al. 2002) or at the moment of the “trigger spike” (e.g. Rothstein et al. 2005), it seems reasonable to assume that the dip in the lightcurve coincides with changes in the structure of the inner disc that ultimately lead to the ejection of a synchrotron blob. These same changes may therefore hide a significant fraction of the central X-ray luminosity from the wind-producing outer disc.

As for the relative timing of the disc and wind variability, we note that the  $\beta$  state is associated with periodic changes in the disc mass accretion rate (e.g. Migliari & Belloni 2003), whether or not their origin is completely understood. It is expected that mass accretion rate and scale height in the inner disc can evolve on viscous and thermal time-scales, respectively (Frank, King, & Raine 2002). The thermal time-scale is comparable to the dynamical time-scale, so the scale height of the disc can change rapidly relative to the accretion rate at any radius. To be quantitative, we consider the radius  $R_{\text{visc}}$  at which the viscous time  $t_{\text{visc}}$  is equal to the  $\beta$  state’s 30-minute cycle (i.e. we assume that the  $\beta$  state is in part a viscous instability like many other states of GRS 1915+105; e.g. Nayakshin, Rappaport, & Melia 2000). Using Equation 1 of Belloni et al. (1997), we find that  $R_{\text{visc}} \lesssim 7 \times 10^9$  cm even if  $\dot{M}$  is as high as  $10^{20}$  g s $^{-1}$  (assuming a viscosity parameter  $\alpha = 0.01$  and black hole mass  $M = 14 M_{\odot}$ ). At this radius, the thermal time-scale is  $\sim 0.1$  second. Thus any part of the disc participating in 30-minute viscous variations can change its scale height almost instantly, and in any case on time-scales much shorter than the duration of the X-ray dip. Furthermore, we know that winds driven by thermal and radiation pressure can respond to changes in the luminosity in as few as five seconds (Paper II). Therefore, we conclude that our shadowing explanation is plausible.

If this scenario is correct, it would explain the uncanny ability of the wind to “know” about the state of the inner disc, i.e. why winds might be preferentially formed when jets are absent. Because the radiation from the disc launches the wind, the wind can effectively respond to changes in the driving luminosity *as they occur*. There may be delays due to light travel time, but this is only a few seconds and is short compared to the duration of the dip. In short, the remarkable quenching of the wind during the hard X-ray dip is a clear consequence of the radiative links between the inner and outer parts of the accretion flow, consistent with our results for the heartbeat state on time-scales of 5 seconds (Neilsen et al. 2011).

## 5.2 Flux-resolved studies

The complex radiative links between the wind and the inner and outer accretion disc are also apparent in the flux dependence of the properties of the wind absorption lines. For the  $\beta$  and  $\gamma$  states, we summarize our results in Figure 7. Note that any two points in Figure 7 that have the same symbol and fill style are statistically independent. At this level, we do not have the signal to statistically distinguish changes in the wind speed, but this figure clearly demonstrates that the

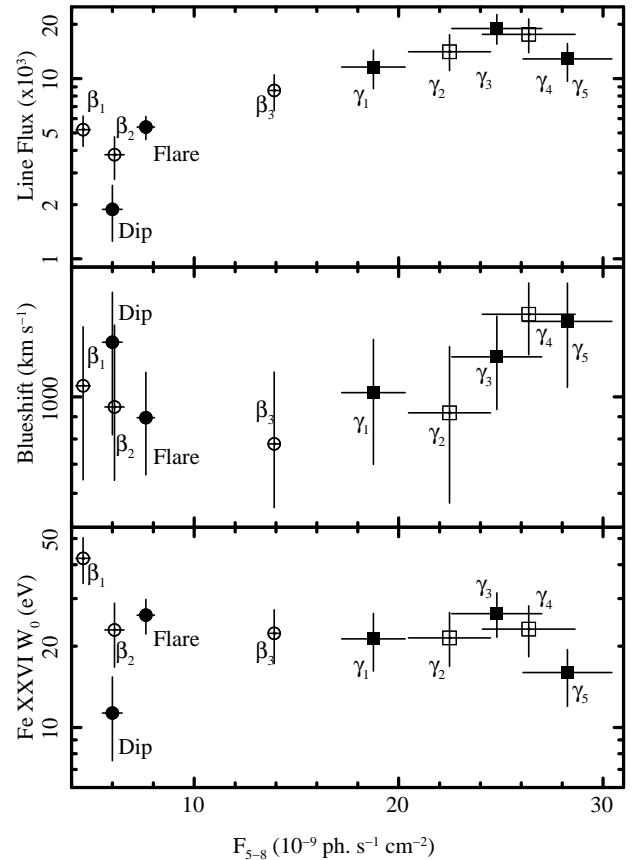


**Figure 7.** Flux-resolved properties of the accretion disc wind in the  $\beta$  and  $\gamma$  states of GRS 1915+105. The  $\beta$  state points are marked with circles, while the results for the  $\gamma$  state are marked with squares. For a given state, symbols with the same fill style are statistically independent. Top panel: the Fe XXVI line flux, which generally increases with increasing continuum flux. Middle panel: the wind blueshift, which is consistent with a constant over all flux. Bottom panel: the Fe XXVI equivalent width, which is mostly constant; see Section 5 for a discussion of deviations from a constant equivalent width.

line flux and equivalent width exhibit a dependence on the observed continuum flux that is non-linear and not necessarily even monotonic.

Part of this non-linearity is due to the behavior discussed in Section 5.1, in which residual absorption lines from a wind launched in some previous epoch may still be present in the X-ray spectrum. As discussed in the preceding section, wind driving may be sensitive to both the X-ray luminosity and the state and structure of the inner accretion flow.

For the most part, the line flux rises smoothly and the equivalent width is remarkably constant over a factor of nearly five in continuum flux. This would seem to indicate that the Fe XXVI column density changes very slowly with luminosity, even across different states. A direct comparison between  $\beta$  and  $\gamma$  is difficult because of possible changes in line saturation, and because the lines are generally resolved in the  $\gamma$  state but generally not in the  $\beta$  state. Nevertheless, the smooth evolution of the wind properties suggests a common origin (i.e. radiative/thermal driving), in which case we can expect the accretion disc wind and the continuum flux to be strongly linked.

For example, the weakness or absence of Fe XXV in the  $\gamma$  spectra (relative to  $\beta$ ) does suggest that as the X-ray luminosity increases, the wind does become progressively more ionized. This conclusion is supported by the behavior of the Fe XXV/Fe XXVI ratio in our flux-resolved  $\beta$  flare spectra. In addition, because the abundance of Fe XXVI should drop sharply due to over-ionization above some critical luminosity, we believe the drop in the Fe XXVI line flux and equivalent width after  $\gamma_3$  (Figure 7) further reinforce the conclusion that the X-ray luminosity is a major determining factor of the wind properties.

On the other hand, it remains clear that there is more to disc winds than the luminosity that drives them. For example, the density of the wind in GRS 1915+105 seems to be independent of luminosity at around  $10^{12} \text{ cm}^{-3}$  (Lee et al. 2002; Ueda et al. 2009; Neilsen et al. 2011; this work). Or consider that the equivalent width of the iron line is highest in  $\beta_1$ , which has the lowest continuum flux studied in this work. It may be that different driving mechanisms are important at different luminosities, i.e. MHD winds (Proga 2000; Miller et al. 2006a, 2008), or it may be that flux-resolved studies like the one presented here fail to capture the true time-dependence of variable winds. In the heartbeat state, the wind is launched *by* high luminosities but doesn't rise into our line of sight until after the X-ray luminosity has fallen (Paper II); the same may also be true during the  $\beta$  flares and the  $\gamma$  state, whose variability is even more erratic.

## 6 CONCLUSIONS

In this paper, we have presented a time- and flux-resolved high-resolution spectral analysis of GRS 1915+105 in the  $\beta$  and  $\gamma$  states. Although only the  $\beta$  state is associated with transient jet formation, both states exhibit strong erratic X-ray variability, which we have used to probe the relationship between the central X-ray luminosity and the properties of the accretion disc wind. In particular, our new results confirm our previous finding that radiation mediates rapid interactions between the inner accretion disc and the outer accretion disc. This interaction is most evident in the  $\beta$  state, where the wind is actually quenched during the hard X-ray dip, possibly because the irradiation of the outer disc is affected by changes in the structure of the inner disc leading to the formation of a transient jet. To the best of our knowledge, this is the first time that a wind has been observed to turn off within a single observation, and the mechanism ( $\dot{M}$  and/or structural changes in the inner disc) requires intricate links between radiation, winds, and jets.

This result is therefore an exciting step towards a complete understanding of wind-jet interactions on all time-scales. With our sensitivity and limited time resolution, our best estimates place the wind in the  $\beta$  state  $\sim 10^{11} \text{ cm}$  from the black hole, leaving it effectively unable to affect the transient jet on such short time-scales. However, if future multiwavelength studies unaffected by telemetry saturation are able to place better constraints on the location of the wind, and require it to be very close to the black hole, then the  $\beta$  state might produce the first evidence for direct wind-jet interactions on any time scale. Such a result would significantly enhance our understanding of accretion and ejection as profoundly inter-related processes around black holes.

## ACKNOWLEDGEMENTS

We thank the referee for comments that improved the clarity of our presentation. We thank Ron Remillard and Claude Canizares for helpful discussions of spectral variability. J.N. and J.C.L. gratefully acknowledge funding support from *Chandra* grant AR0-11004X, the Harvard University Graduate School of Arts and Sciences, and the Harvard University Faculty of Arts and Sciences. J.N. acknowledges additional support from the National Aeronautics and Space Administration through the Smithsonian Astrophysical Observatory contract SV3-73016 to MIT for support of the *Chandra* X-ray Center, which is operated by the Smithsonian Astrophysical Observatory for and on behalf of the National Aeronautics Space Administration under contract NAS8-03060.

## REFERENCES

- Begelman, M. C., McKee, C. F., & Shields, G. A. 1983, *ApJ*, 271, 70
- Belloni, T., Klein-Wolt, M., Méndez, M., van der Klis, M., & van Paradijs, J. 2000, *A&A*, 355, 271
- Belloni, T., Méndez, M., King, A. R., van der Klis, M., & van Paradijs, J. 1997, *ApJL*, 488, L109+
- Blum, J. L., Miller, J. M., Cackett, E., Yamaoka, K., Takahashi, H., Raymond, J., Reynolds, C. S., & Fabian, A. C. 2010, *ApJ*, 713, 1244
- Brandt, W. N., & Schulz, N. S. 2000, *ApJL*, 544, L123
- Canizares, C. R., et al. 2005, *PASP*, 117, 1144
- Draine, B. T. 2011, *Physics of the Interstellar and Inter-galactic Medium*, ed. Draine, B. T.
- Ebisawa, K. 1997, in *X-Ray Imaging and Spectroscopy of Cosmic Hot Plasmas*, ed. F. Makino & K. Mitsuda, 427–+
- Eikenberry, S. S., Matthews, K., Morgan, E. H., Remillard, R. A., & Nelson, R. W. 1998, *ApJL*, 494, L61+
- Fender, R., & Belloni, T. 2004, *ARA&A*, 42, 317
- Fender, R. P., Belloni, T. M., & Gallo, E. 2004, *MNRAS*, 355, 1105
- Fender, R. P., Garrington, S. T., McKay, D. J., Muxlow, T. W. B., Pooley, G. G., Spencer, R. E., Stirling, A. M., & Waltman, E. B. 1999, *MNRAS*, 304, 865
- Fender, R. P., Pooley, G. G., Brocksopp, C., & Newell, S. J. 1997, *MNRAS*, 290, L65
- Frank, J., King, A., & Raine, D. J. 2002, *Accretion Power in Astrophysics: Third Edition* (Cambridge, UK: Cambridge University Press)
- Hannikainen, D. C., et al. 2005, *A&A*, 435, 995
- Houck, J. C. 2002, in *High Resolution X-ray Spectroscopy with XMM-Newton and Chandra*, ed. G. Branduardi-Raymont
- Houck, J. C., & Denicola, L. A. 2000, in *Astronomical Society of the Pacific Conference Series*, Vol. 216, *Astronomical Data Analysis Software and Systems IX*, ed. N. Manset, C. Veillet, & D. Crabtree, 591–+
- Kallman, T., & Bautista, M. 2001, *ApJS*, 133, 221
- Kallman, T. R., Bautista, M. A., Goriely, S., Mendoza, C., Miller, J. M., Palmeri, P., Quinet, P., & Raymond, J. 2009, *ApJ*, 701, 865
- Klein-Wolt, M., Fender, R. P., Pooley, G. G., Belloni, T., Migliari, S., Morgan, E. H., & van der Klis, M. 2002, *MNRAS*, 331, 745
- Kotani, T., Ebisawa, K., Dotani, T., Inoue, H., Nagase, F., Tanaka, Y., & Ueda, Y. 2000a, *ApJ*, 539, 413

- Kotani, T., et al. 2000b, *Advances in Space Research*, 25, 445
- Kotani, T., et al. 1997, in *American Institute of Physics Conference Series*, Vol. 410, *Proceedings of the Fourth Compton Symposium*, ed. C. D. Dermer, M. S. Strickman, & J. D. Kurfess, 922–926
- Lee, J. C., Reynolds, C. S., Remillard, R., Schulz, N. S., Blackman, E. G., & Fabian, A. C. 2002, *ApJ*, 567, 1102
- Luketic, S., Proga, D., Kallman, T. R., Raymond, J. C., & Miller, J. M. 2010, *ApJ*, 719, 515
- Markwardt, C. B., Swank, J. H., & Taam, R. E. 1999, *ApJL*, 513, L37
- Meier, D. L. 2001, *ApJL*, 548, L9
- Migliari, S., & Belloni, T. 2003, *A&A*, 404, 283
- Mikles, V. J., Eikenberry, S. S., & Rothstein, D. M. 2006, *ApJ*, 637, 978
- Miller, J. M., Maitra, D., Cackett, E. M., Bhattacharyya, S., & Strohmayer, T. E. 2011, *ApJL*, 731, L7+
- Miller, J. M., Raymond, J., Fabian, A., Steeghs, D., Homan, J., Reynolds, C., van der Klis, M., & Wijnands, R. 2006a, *Nature*, 441, 953
- Miller, J. M., et al. 2004, *ApJ*, 601, 450
- . 2006b, *ApJ*, 646, 394
- Miller, J. M., Raymond, J., Reynolds, C. S., Fabian, A. C., Kallman, T. R., & Homan, J. 2008, *ApJ*, 680, 1359
- Mirabel, I. F., Dhawan, V., Chaty, S., Rodriguez, L. F., Marti, J., Robinson, C. R., Swank, J., & Geballe, T. 1998, *A&A*, 330, L9
- Mirabel, I. F., & Rodríguez, L. F. 1999, *ARA&A*, 37, 409
- Nayakshin, S., Rappaport, S., & Melia, F. 2000, *ApJ*, 535, 798
- Neilsen, J., & Lee, J. C. 2009, *Nature*, 458, 481
- Neilsen, J., Remillard, R. A., & Lee, J. C. 2011, *ApJ*, 737, 69
- Ponti, G., Fender, R., Begelman, M., Dunn, R. J. H., Coriat, M., Neilsen, J., & Coriat, M. 2011, *MNRAS*, submitted
- Pooley, G. G., & Fender, R. P. 1997, *MNRAS*, 292, 925
- Proga, D. 2000, *ApJ*, 538, 684
- Proga, D., & Kallman, T. R. 2002, *ApJ*, 565, 455
- Reynolds, M. T., & Miller, J. M. 2010, *ApJ*, 723, 1799
- Rodriguez, J., et al. 2008a, *ApJ*, 675, 1436
- . 2008b, *ApJ*, 675, 1449
- Rothstein, D. M., Eikenberry, S. S., & Matthews, K. 2005, *ApJ*, 626, 991
- Schulz, N. S., & Brandt, W. N. 2002, *ApJ*, 572, 971
- Shields, G. A., McKee, C. F., Lin, D. N. C., & Begelman, M. C. 1986, *ApJ*, 306, 90
- Soleri, P., Belloni, T., & Casella, P. 2008, *MNRAS*, 383, 1089
- Steiner, J. F., McClintock, J. E., Remillard, R. A., Narayan, R., & Gou, L. 2009, *ApJL*, 701, L83
- Tagger, M., Varnière, P., Rodriguez, J., & Pellat, R. 2004, *ApJ*, 607, 410
- Ueda, Y., et al. 2010, *ApJ*, 713, 257
- Ueda, Y., Murakami, H., Yamaoka, K., Dotani, T., & Ebisawa, K. 2004, *ApJ*, 609, 325
- Ueda, Y., Yamaoka, K., & Remillard, R. 2009, *ApJ*, 695, 888
- Verner, D. A., Ferland, G. J., Korista, K. T., & Yakovlev, D. G. 1996, *ApJ*, 465, 487
- Wilms, J., Allen, A., & McCray, R. 2000, *ApJ*, 542, 914
- Xiang, J., Lee, J. C., Nowak, M. A., Wilms, J., & Schulz, N. S. 2009, *ApJ*, 701, 984
- Zdziarski, A. A., Johnson, W. N., & Magdziarz, P. 1996, *MNRAS*, 283, 193
- Zimmerman, E. R., Narayan, R., McClintock, J. E., & Miller, J. M. 2005, *ApJ*, 618, 832
- Życki, P. T., Done, C., & Smith, D. A. 1999, *MNRAS*, 309, 561

This paper has been typeset from a  $\text{\LaTeX}$  file prepared by the author.